Research Article Vol. 9, No. 3 / March 2022 / Optica 295

Phase retrieval framework for direct reconstruction of the projected refractive index applied to ptychography and holography

Felix Wittwer,[1,2,3,†,*] Johannes Hagemann,[1,4,†] Dennis Brückner,[1,2,4] Silja Flenner,[5] and Christian G. Schroer[1,2,4]

[1]CXNS — Center for X-ray and Nano Science CXNS, Deutsches Elektronen-Synchrotron DESY, Notkestraße 85, 22607 Hamburg, Germany
[2]Department Physik, Universität Hamburg, Luruper Chaussee 149, 22761 Hamburg, Germany
[3]Current address: NERSC, Lawrence Berkeley National Laboratory, Berkeley, California 94720, USA
[4]Helmholtz Imaging Platform, Deutsches Elektronen-Synchrotron DESY, Notkestraße 85, 22607 Hamburg, Germany
[5]Helmholtz-Zentrum Hereon, Max-Planck-Str. 1, 21502 Geesthacht, Germany
*Corresponding author: wittwer@xray-lens.de

Received 26 October 2021; revised 1 February 2022; accepted 2 February 2022; published 9 March 2022

The interaction of an object with a coherent probe often encodes its properties in a complex-valued function, which is then detected in an intensity-only measurement. Phase retrieval methods commonly infer this complex-valued function from the intensity. However, the decoding of the object from the complex-valued function often involves some ambiguity in the phase, e.g., when the phase shift in the object exceeds 2π. Here, we present a phase retrieval framework to directly recover the amplitude and phase of the object. This refractive framework is straightforward to integrate into existing algorithms. As examples, we introduce refractive algorithms for ptychography and near-field holography and demonstrate this method using measured data.

https://doi.org/10.1364/OPTICA.447021

1. INTRODUCTION

Phase retrieval (PR), i.e., the recovery of a complex-valued signal from intensity-only measurements, is a ubiquitous task in physics and engineering [1–5]. It is used wherever detectors are not fast enough to measure the oscillations of a signal of interest. PR is therefore especially prevalent in electron [6] and x-ray microscopy [7–10], but it also finds applications in terahertz imaging [11] and optical microscopy [12]. Today, a wide range of PR techniques has been developed to image samples in different experimental situations [13–15].

Commonly, the object of interest is nearly transparent and shows little attenuation contrast. This is a frequent problem in the imaging of biological specimens, where the object imprints only a phase shift on the transmitted wave [16,17]. The phase shift is therefore often more important to image the sample than the attenuation. Notably, PR allows to recover the attenuation and the phase shift of the sample, which makes PR ideally suited to image otherwise invisible objects. Phase contrast techniques such as speckle tracking [18], grating interferometry [19], diffraction-enhanced imaging [20], or edge enhancement [21] allow one to directly measure the refractive index of the sample. However, these methods lack the increase in resolution that PR techniques such as holography [22] or ptychography [23] offer.

Conventional PR typically reconstructs the complex wave field behind the object [24]. The phase shift induced by the object is then recovered from this wave field. For thick samples with large phase shifts, the recovered phase is wrapped to a range of 2π. The wrapped phase is problematic for tomography as it requires a dedicated reconstruction algorithm [25]. Furthermore, the tomography algorithm has problems if the reconstructed phase projections contain phase singularities [26,27].

An alternative way that avoids the problematic phase unwrapping altogether has been proposed by Chowdhury *et al.* for Fourier ptychography [28]. In general, PR methods recover the complex transmission of the sample. Instead of the transmission, the proposed refractive framework directly reconstructs the projected refractive index of the sample. The projection is the logarithm of the transmission, scaled by the wavenumber $k = 2\pi/\lambda$, where λ is the wavelength of the light or electrons. Particularly, the projected refractive index is no longer bound to a range of 2π and is linearly related to the refractive index. This last property is beneficial for complex PR schemes that couple multiple scans into one reconstruction [29–31].

In this work, we generalize the idea of refractive PR and apply it to two popular PR techniques: ptychography [23,32] and near-field holography (NFH) [22,33]. As this approach is very general, it can be applied to other PR algorithms. In Section 2, this general idea is described for how refractive variants for other PR algorithms can be constructed. We demonstrate the performance of refractive ptychography and refractive holography on experimental

data from x-ray microscopy experiments measured at beamlines P05 and P06 of the synchrotron radiation source PETRA III in Hamburg, Germany. While these demonstrations all use hard x rays, all arguments are transferable to other probes, such as other electromagnetic waves and electrons.

2. REFRACTIVE FRAMEWORK

A. Object Representation for Phase Retrieval

The refractive index n of a material describes how it interacts with light or x rays. Specifically, it specifies how much the wave is slowed down and how much it is attenuated. For imaging applications, the focus is often on the contrast between different refractive indices. As only this contrast is important, it is useful to write the refractive index as the difference between the material and the vacuum:

$$n = 1 - \delta + \mathrm{i}\beta. \tag{1}$$

Here, the refractive index decrement δ represents the change in phase velocity, and β describes the attenuation in the material compared to the vacuum.

For a thin sample, the imaging contrast at a point $\mathbf{r} = (x, y)$ is given by the object transmission function

$$O_{\mathbf{r}} = A_{\mathbf{r}} \cdot \exp(\mathrm{i}\Phi_{\mathbf{r}}) = \exp\left(\mathrm{i}k \int (n-1)\mathrm{d}z\right), \tag{2}$$

which projects the refractive index along the optical axis z. The goal of conventional PR is to recover $O_{\mathbf{r}}$. For refractive PR, the aim is to reconstruct the refractive object function

$$\tilde{O}_{\mathbf{r}} = k \int (n-1)\mathrm{d}z = -k \int \delta \mathrm{d}z + \mathrm{i}k \int \beta \mathrm{d}z. \tag{3}$$

This function is related to the object transmission function $O_{\mathbf{r}}$ through a complex exponential:

$$O_{\mathbf{r}} = \exp(\mathrm{i}\tilde{O}_{\mathbf{r}}). \tag{4}$$

Due to this relationship, the phase shift $\Phi_{\mathbf{r}}$ and the amplitude $A_{\mathbf{r}}$ are associated respectively with the real and imaginary components of the refractive object function:

$$\Phi_{\mathbf{r}} = \Re(\tilde{O}_{\mathbf{r}}) = -k \int \delta \mathrm{d}z, \tag{5}$$

$$-\ln(A_{\mathbf{r}}) = \Im(\tilde{O}_{\mathbf{r}}) = k \int \beta \mathrm{d}z. \tag{6}$$

Since PR algorithms recover the real and imaginary parts of the object transmission function $O_{\mathbf{r}}$, the phase shift $\Phi_{\mathbf{r}}$ has to be calculated from the reconstruction. In this case, this phase shift is the argument of a complex number and is wrapped to a range of 2π. Any larger values can be reconstructed only through unwrapping. In refractive PR, $\Phi_{\mathbf{r}}$ is directly reconstructed, avoiding phase wraps altogether.

In electron microscopy, the imaging contrast of a sample can also be described with the amplitude and phase shift of a complex transmission function [17,34]. Thus, the refractive framework can be applied analogously to the PR of electron waves.

B. Refractive Phase Retrieval

The object is reconstructed by solving the phase problem. To solve the latter, most PR algorithms follow an error reduction strategy that aims at minimizing the error d between the measured diffraction images M_j and modeled images I_j. Popular choices for d are the euclidean metric or a log-likelihood function. The specific choice for d is not important for this discussion as the argument is true for all metrics. The I_j are determined by modeling the diffraction process based on the current object transmission function. The error reduction strategy is based on the assumption that as the error goes to zero, the approximate object transmission function will converge to the true object transmission function. In each iteration, the object is updated so that the error sum

$$L = \sum_{j=1}^{J} d(I_j, M_j) \tag{7}$$

of all J diffraction patterns M_j is reduced. The improvement is determined by the gradient of the total error L.

For the refractive framework, we switch the model function of the object from the object transmission function [Eq. (2)] to the refractive object function [Eq. (3)]. The gradient for refractive PR can be calculated using Wirtinger derivatives [35] with respect to the refractive object function:

$$\frac{\partial L}{\partial \tilde{O}_{\mathbf{r}}} = \frac{\partial L}{\partial O_{\mathbf{r}}} \cdot \frac{\partial O_{\mathbf{r}}}{\partial \tilde{O}_{\mathbf{r}}} = \frac{\partial L}{\partial O_{\mathbf{r}}} \cdot \mathrm{i}O_{\mathbf{r}}. \tag{8}$$

In essence, the refractive gradient is nearly identical to the conventional gradient, except for a simple multiplication with the imaginary unit and the object transmission function $O_{\mathbf{r}}$. Significantly, this is true for any error reduction algorithm, as we did not specify any concrete error function or image forming process. As a result, many conventional PR algorithms can be readily converted to the refractive framework by simply multiplying the object update with $\mathrm{i}O_{\mathbf{r}}$. We demonstrate this in the following sections by presenting refractive algorithms for ptychography and holography.

3. REFRACTIVE PTYCHOGRAPHY

A. Refractive Ptychographic Phase Retrieval Algorithm

Ptychography combines scanning microscopy with coherent diffraction imaging to solve the phase problem [13,23]. A typical ptychographic scanning setup is shown in Fig. 1(a). To reconstruct the refractive object function from the diffraction patterns, we introduce here the refractive ptychographic iterative engine (refPIE), an advancement of the widely used extended PIE (ePIE) [36]. A detailed derivation of refPIE is given in [37]. Refractive extensions to other algorithms such as 3PIE [38], multi-modal ptychography [39], etc., can be obtained straightforwardly, using refPIE as a template.

Similar to ePIE and other ptychography algorithms [23], refPIE starts from initial guesses $\tilde{O}_0$ and P_0 for the refractive object and probe function. In the reconstruction, the update steps are repeated until $\tilde{O}$ and P converge.

1. Randomly choose a diffraction pattern M_j that was not yet processed.
2. Using the corresponding scan point $\mathbf{R}_j$, calculate the exit wave:

$$\psi_{\mathbf{r}} = \exp(\mathrm{i}\tilde{O}_{\mathbf{r}}) \cdot P_{\mathbf{r}-\mathbf{R}_j}. \tag{9}$$

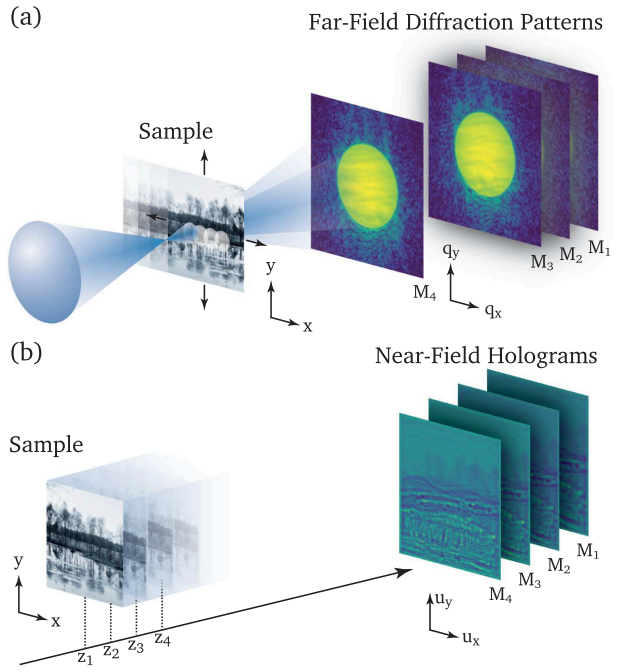

Fig. 1. Experimental setups for (a) ptychography and (b) inline holography. (a) In ptychography, the sample is scanned transversal to the beam direction. For each scan point $\mathbf{R}_j$, the detector records the far-field diffraction pattern M_j. For a successful reconstruction, the beam footprints from adjacent scan points should overlap. This ensures that the corresponding diffraction patterns share information. (b) In holography, the sample is moved along the beam direction to different defocus distances z_j, each giving rise to a different hologram M_j due to the change in the Fresnel number Fr_j.

3. Propagate the scattered wave to the detector, using the Fourier transform (far field) or Fresnel propagation (near field):

$$\Psi_{\mathbf{q}} = \mathcal{F}(\psi_{\mathbf{r}}). \tag{10}$$

4. Replace the modeled amplitude with the measured diffraction pattern, keeping only the phase of Ψ:

$$\Psi'_{\mathbf{q}} = \sqrt{M_{j,\mathbf{q}}} \cdot \frac{\Psi_{\mathbf{q}}}{|\Psi_{\mathbf{q}}|}. \tag{11}$$

5. Propagate the updated wave back to the sample plane:

$$\psi'_{\mathbf{r}} = \mathcal{F}^{-1}(\Psi'_{\mathbf{q}}). \tag{12}$$

6. At the end, update the refractive object and probe function with the updated exit wave (parameters α and β tune the update strength):

$$\tilde{O}_{\mathbf{r}} \leftarrow \tilde{O}_{\mathbf{r}} + \alpha \frac{\left(\mathrm{i}\psi_{\mathbf{r}-\mathbf{R}_j}\right)^*}{\max |\psi_{\mathbf{r}-\mathbf{R}_j}|^2} \cdot \left(\psi'_{\mathbf{r}} - \psi_{\mathbf{r}}\right), \tag{13a}$$

$$P_{\mathbf{r}} \leftarrow P_{\mathbf{r}} + \beta \frac{\exp\left(-\mathrm{i}\tilde{O}^*_{\mathbf{r}+\mathbf{R}_j}\right)}{\max \left|\exp\left(\mathrm{i}\tilde{O}_{\mathbf{r}+\mathbf{R}_j}\right)\right|^2} \cdot \left(\psi'_{\mathbf{r}} - \psi_{\mathbf{r}}\right). \tag{13b}$$

One iteration is complete when there are no more diffraction patterns to process. Before the next iteration starts, all patterns are again marked as unprocessed. Typically, the reconstruction converges after 100 up to 1000 iterations.

Most steps of refPIE are identical to those in other ptychography algorithms. The unique difference and central feature of refPIE is Eq. (13a), where the difference $\psi' - \psi$ is conventionally multiplied with the complex conjugated probe P. Here, P is replaced with $\mathrm{i}\psi$, the exit wave multiplied with the imaginary unit. The proof that this exchange leads to a refractive reconstruction follows from Eq. (8) as $P \cdot \mathrm{i}O = \mathrm{i}\psi$. The complex conjugation is due to the nature of Wirtinger derivatives.

B. Micrometeorite Experiment

We demonstrate the capabilities of refPIE on a ptychography scan of a micrometeorite. The experiment was carried out at beamline P06 of PETRA III (DESY, Hamburg), using the combined Micro-Nanoprobe setup to maximize the detector distance [40]. The 18 keV x-ray beam was focused by a pair of Kirkpatrick–Baez (KB) mirrors, focal length 250 mm, to a full-width at half maximum (FWHM) spot size of 110 nm × 110 nm, as obtained from the ptychographic reconstruction. The sample was placed 500 µm behind the focus where the beam had expanded to a FWHM size of 300 nm × 200 nm (h × v). The micrometeorite has a diameter of about 80 µm. To quickly scan a sample of this size, the scanning stage never stopped, and moved the micrometeorite in a continuous zigzag path across the beam. These fly-scans allow acquisition rates in the kilohertz range [41–44]. The micrometeorite was scanned over a 100 µm × 100 µm area with 1 ms exposure for each diffraction pattern. The velocity of the stage was set to 200 µm s^{-1} so that the micrometeorite moved 200 nm during one exposure. Each new line was vertically offset by the same amount of 200 nm. While the probe overlap in the vertical direction is below the empirical optimum, there is still sufficient overlap due to the cross-shape of the KB-focus. The scan recorded more than a quarter of a million diffraction patterns in under 9.5 min. The diffraction patterns were recorded with an Eiger 500 k situated 8.75 m downstream of the sample in the Nanoprobe hutch. A 7 m long evacuated flight tube between sample and detector reduced air scattering on the detector. The reconstructions use the central 128 × 128 pixels of the Eiger images, resulting in a pixel size of 62.8 nm in the ptychographic reconstruction. All experimental parameters are summarized in Table 1.

For comparison, we reconstructed the meteorite using both ePIE and refPIE. Since the probe is very small compared to the scan size, both algorithms converge slowly. To improve the reconstruction speed, we similarly modified both algorithms. First, we adapted the parallel ptychography variant described in [45,46] for ePIE and refPIE. As suggested in [47], we keep the intensity of the probe during the reconstruction fixed to the photon count of the brightest diffraction pattern. We also constrained the object modulus to a range from 0.2 to 2.0. Experience has shown that it

Table 1. Parameters of the Micrometeorite Experiment

Parameters	Value
Energy	18 keV
Flux	3.75×10^8/s
Exposure	1 ms
Scan size	100 µm × 100 µm
Step size	200 nm × 200 nm
Probe size (h × v)	300 nm × 200 nm
Detector distance	8752 mm
Detector pixel	75 µm × 75 µm
Image size	128 × 128 pixels
Pixel size (rec.)	62.8 nm

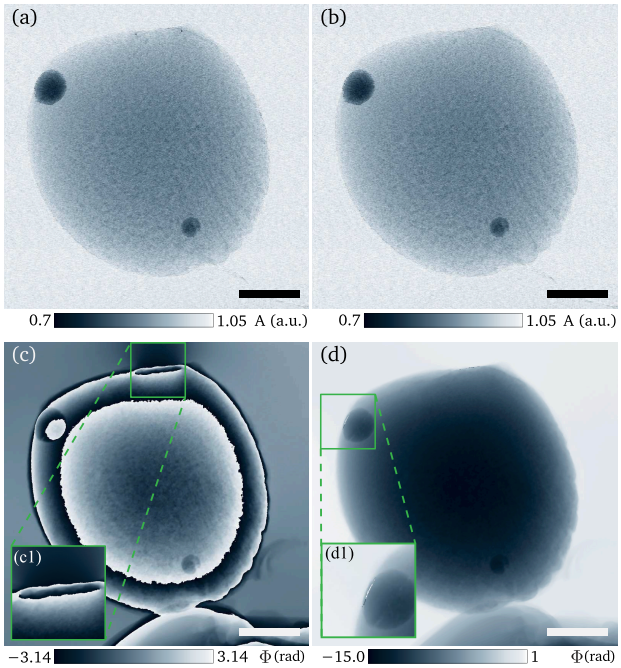

Fig. 2. Ptychographic reconstruction of the micrometeorite. (a), (b) Moduli of the micrometeorite obtained by ePIE and refPIE, respectively. (c), (c1) Phase of the ePIE reconstruction. The reconstruction shows strong phase wrapping and the detail (c1) shows a pair of phase vortices. (d), (d1) Phase of the refPIE reconstruction. The phases are in correct range without any unwrapping applied. The detail (d1) shows an artifact in the top left of the refPIE reconstruction. This artifact is offset by $\pm 2\pi$ to the rest of the meteorite and can easily be fixed. The scale bars represent 20 μm.

benefits the reconstruction if the algorithm is allowed to overshoot. And last we used momentum accelerated gradients for both algorithms, as described in [47–49]. In both reconstructions, we set the momentum damping factors η_{obj} and η_{prb} to 0.98 and applied the momentum in every second iteration. The object and probe update strengths α and β were both set to 1.0.

Both algorithms ran for 1000 iterations, and the reconstructed sample amplitudes and phase shifts are shown in Fig. 2. The ePIE reconstruction shows phase wraps and two phase vortices at the top of the meteorite, shown in the inset. These singularities are especially problematic for tomographic reconstructions. While pairs of vortices of opposite helicity have the tendency to self-annihilate during reconstruction, there is the chance that this occurs only after an impractically large number of iterations. In contrast, the discontinuities and phase wrap problems are solved in the refPIE reconstruction. The real part, shown in Fig. 2(d), is continuous and shows no phase wrapping, despite a maximum phase shift of close to 15 rad. Two small areas at the top and the left contain offset values; see Fig. 2(d1). These areas have the largest phase gradients in the reconstruction, up to 2 rad per pixel. Both ePIE and refPIE struggle in the reconstruction of these sample areas. For refPIE, these areas are offset by 2π, which can be fixed, for example, with the numpy *unwrap* function. In both cases, refPIE is able to isolate problematic regions and reconstruct the unaffected parts of the sample without detriments.

In contrast, directly unwrapping the ePIE reconstruction is challenging, as shown in Fig. 3. While the phase offsets in refPIE are corrected with numpy *unwrap*, in ePIE, three of the four unwrapping methods fail altogether to remove the artifacts. Only by first removing all vortices, as described in [26], and then correcting any phase offsets with numpy *unwrap*, is the result nearly artifact free. Still, small differences remain in comparison to refPIE; see Fig. 3(e). One difference is the background inside the green square, which is notably darker in Fig. 3(d2). This long-range difference extends also into the micrometeorite. These problems can potentially be avoided by unwrapping the object after each ePIE iteration. Compared to the refractive update, unwrapping methods are computationally more expensive, as they calculate the phase from the real and imaginary part before the unwrapping can begin.

4. REFRACTIVE NEAR-FIELD HOLOGRAPHY

A. Refractive Phase Retrieval Algorithm in Near-Field Holography

NFH is a full-field imaging scheme that can be implemented in a parallel beam setting or, to achieve higher magnifications and

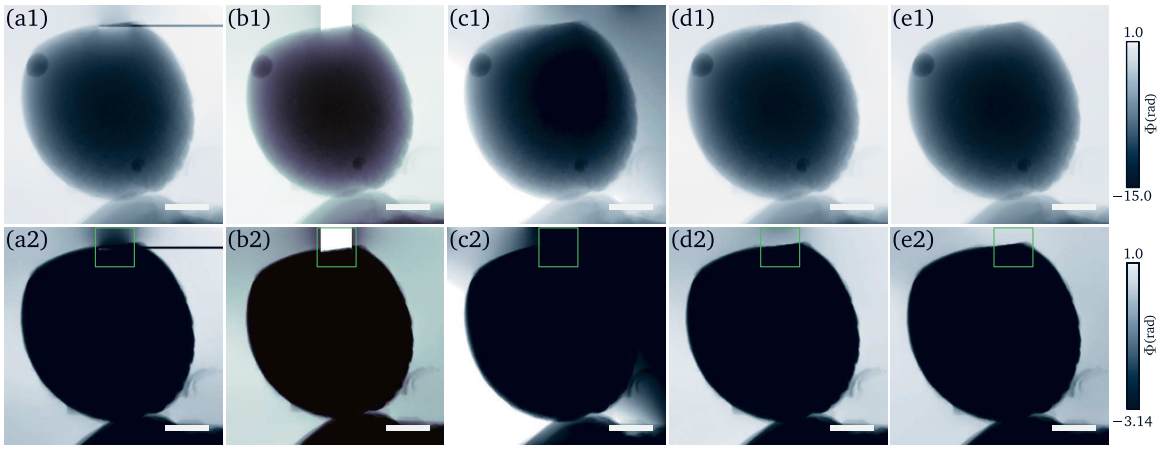

Fig. 3. Post-reconstruction unwrapping of the ePIE and refPIE object phases. The first row (a1)–(e1) shows the full phase range, and the second row (a2)–(e2) shows a smaller phase range to highlight differences in the background. The green squares highlight the critical section with the phase vortices. Each column uses a different unwrapping method. (a) ePIE with numpy *unwrap*. (b) ePIE with the method of Cusack and Papadakis [62]. (c) ePIE with the Fourier based unwrapping from Volkov and Zhu [73]. (d) ePIE with vortex removal as described by Stockmar *et al.* [26] followed by numpy *unwrap*. (e) refPIE with numpy *unwrap*. The scale bars represent 20 μm.

using optical magnification, in conical beam geometry. A principle sketch of a NFH setup in parallel beam geometry is shown in Fig. 1(b). Note that the geometries do not need to be treated separately since the diverging beam setting can be converted in an equivalent parallel beam geometry by the Fresnel scaling theorem [50]. NFH allows for single-exposure acquisitions of extended objects and is thus a promising method to image ultra-short processes [51,52] and radiation-sensitive samples [53].

As a basis for the refractive near-field PR, we use an alternating projection (AP) algorithm given by

$$\tilde{O}_{\mathbf{r}} \leftarrow \tilde{P}_S(\tilde{P}_M(\tilde{O}_{\mathbf{r}})), \tag{14}$$

where the sample constraint $\tilde{P}_S$ constricts the reconstruction in the sample plane, and the magnitude projector $\tilde{P}_M$ ensures that the reconstruction fits to the measurement and is defined as

$$\tilde{P}_M(\tilde{O}_{\mathbf{r}}) := \tilde{O}_{\mathbf{r}} - \Delta\tilde{O}_{\mathbf{r}}, \tag{15}$$

where $\Delta\tilde{O}_{\mathbf{r}}$ is specified below. Common object constraint choices are a support, i.e., restricting the object to a certain part of the field of view, or a vanishing attenuation, i.e., assuming the object to be purely phase shifting. These constraints can be readily adapted for the refractive framework. Notably, the homogeneity constraint or single material constraint [21,54] can be directly expressed in the refractive framework as a constant ratio between δ and β or $\Re(\tilde{O})$ and $\Im(\tilde{O})$, respectively. Concerning Eq. (15), the difference from the conventional holography algorithm [55] is the object update

$$\Delta\tilde{O}_{\mathbf{r}} := -\frac{\mathrm{i}O_{\mathbf{r}}^*}{J\ \max|O_{\mathbf{r}}|^2}\sum_{j=1}^{J}\mathcal{D}_{\mathrm{Fr}_j}^{-1}\left(\mathcal{D}_{\mathrm{Fr}_j}(O_{\mathbf{r}})\cdot\left[1-\sqrt{M_j/I_j}\right]\right), \tag{16}$$

where * denotes the complex conjugate, $\mathcal{D}_{\mathrm{Fr}_j}$ is the Fresnel propagator for the respective Fresnel number Fr_j, M_j denotes the measured hologram, $I_j = |\mathcal{D}_{\mathrm{Fr}_j}(O_{\mathbf{r}})|^2$ is the current estimate for M_j, and J is the number of measurements. $\mathcal{D}_{\mathrm{Fr}}$ is implemented via a convolution in Fourier space [56]. Fr_j is calculated with respect to the size of a single pixel Δx, i.e., $\mathrm{Fr} = \Delta x^2/(\lambda z_j)$. For a detailed derivation, we refer to [37]. Equation (17) averages the refractive update from all holograms, yielding an improved resistance against noise. Alternatively, the object can be updated in a sequential manner for each hologram individually. For experimental demonstration, we implemented both variants in the HoloTomoToolbox [57,58].

As in ptychography, reconstructing the low-spatial frequencies requires the most iterations in holography. To accelerate this, we combine Eq. (14) with a Nesterov gradient step [48,49]. We refer to this scheme as refAP.

B. Magnesium Wire Experiment

We demonstrate the capabilities of refractive holography using a sample of biodegradable magnesium wire [59,60]. The NFH data were obtained at the nano branch of beamline P05 operated by the Helmholtz-Zentrum Hereon located at PETRA III at DESY, Hamburg. The holographic mode has been introduced in [61]. The measurement was carried out at a photon energy of $E = 11$ keV. The detector was a Hamamatsu C12849-101U with a 10 µm Gadox scintillator and a pixel size of 6.5 µm. It was placed 19.22 m behind the focus of a Fresnel zone plate with a diameter of 300 µm and an outermost zone width of 50 nm [61]. The sample was placed 437 mm behind the focus in the diverging beam of the Fresnel zone plate to achieve a sufficiently large field of view to fit the whole width of the wire. This yields a 45× magnification with an effective pixel size of 144 nm, and combining these parameters gives $\mathrm{Fr} = 4.33 \times 10^{-4}$. All parameters are summarized in Table 2.

Table 2. Parameters of the Magnesium Wire Experiment

Parameter	Value
Energy	11 keV
Exposure/hologram	1.5 s
Field of view	246 µm × 246 µm
Defocus distance	437 mm
Detector distance	19.22 m
Magnification	45
Detector pixel size	6.5 µm × 6.5 µm
Fresnel number	4.33×10^{-4}
Effective pixel size	144 nm × 144 nm
Image size	2048 × 2048 pixels

As a comparison, we reconstructed the magnesium wire with a conventional algorithm based on AP (convAP) [55] and refAP. Both variants were implemented using the HoloTomoToolbox [57], and reconstruction scripts were added as examples to the repository [58]. Before reconstruction, the holograms were flat-field corrected [see Fig. 4(a)] and outliers were removed. To reduce boundary artifacts during back propagation, the values of the holograms' boundaries were smeared out to an array size of 4096 × 4096 pixels using the *fadeoutImage* function of the HoloTomoToolbox. For refAP, the constraints in the sample plane $\tilde{P}_S$ were a combination of value clamping and support. The allowed ranges were $\Phi \in [-80, 0]$ rad and $\Im(\tilde{O}) \in [-0.005, 0.5]$. Following the clamping, Φ and $\Im(\tilde{O})$ were smoothed with a two pixel wide (FWHM) Gaussian filter. A self-refining support was additionally included. Beginning from the 10th iteration, a threshold of 0.08 rad was applied to Φ every fifth iteration. Afterwards, the support was updated by eroding the reconstruction with a five pixel diameter followed by a dilation of five pixel diameter. The support was updated only for the first 400 iterations; afterwards, it was kept constant for the remaining 10,000 iterations. The conventional reconstruction uses the same strategy as above. Some parameters have to be adapted for the conventional setting, e.g., the $\Im(\tilde{O})$ range was converted to an amplitude range $A \in [0.605\ 1.005]$. To apply smoothing and clamp constraint on the phases, a phase unwrapping [62] had to be applied in every iteration. Thus a phase unwrapping algorithm is integrated in the $\tilde{P}_S$ of convAP.

The results from both reconstructions are shown in Figs. 4(c) and 4(d). Note that these reconstructions were obtained from a *single* measurement as input. The phases obtained from convAP are shown in Fig. 4(c). The edges of the wire are resolved on both sides, and the increase in phase shift towards the center emerges but then fails to recover the correct phase shift. The right edge artifacts stem from vortices that appeared during the reconstruction, which could not be removed by phase unwrapping. On the other hand, the reconstruction obtained with refAP Fig. 4(d) shows a continuous increase in overall phase shift towards the center. This reconstruction shows further the different shell layers we expect the wire to have. The degradation happens due to contact with body-fluid analogs; thus the outermost shell is the degradation layer. The degradation layer is generally composed of different degradation

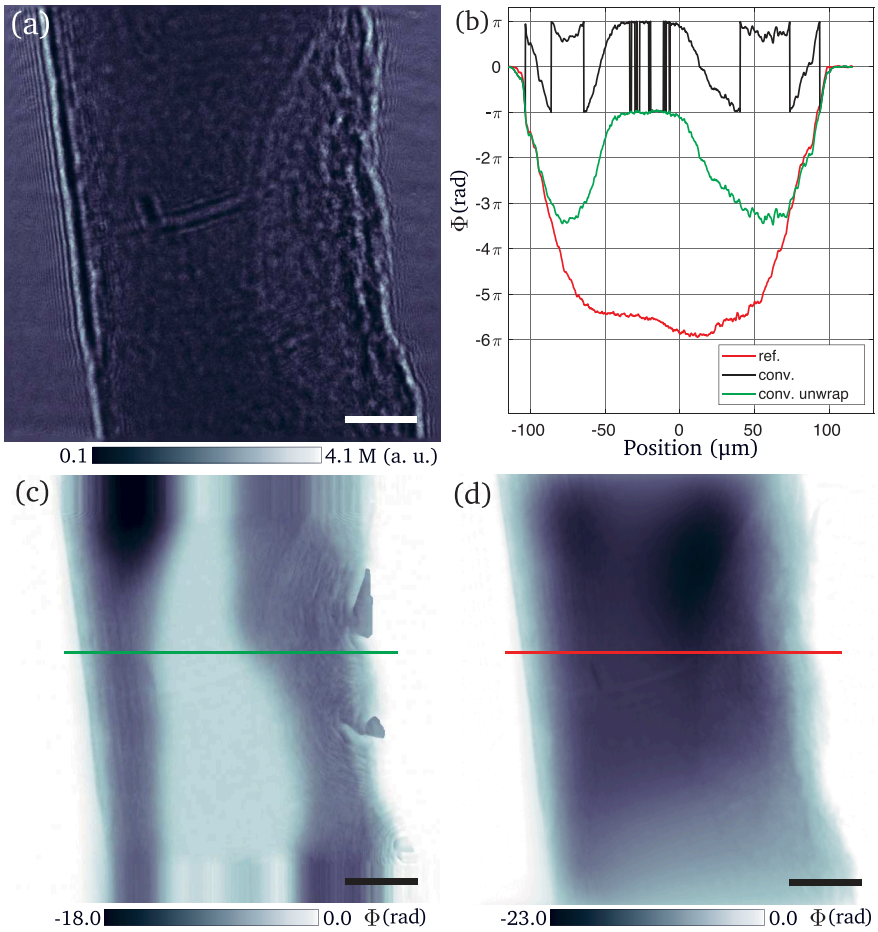

Fig. 4. Results for NFH from experimental data of the magnesium wire. (a) Flat-field corrected hologram of the magnesium wire for 437 mm defocus distance. (b) Line profiles of reconstructed phases. The green and red lines indicate the locations of profiles in conventional and refractive reconstructions, respectively. (c) Phase of conventional reconstruction, not extending to the full phase range. (d) Phase of refractive reconstruction, spanning a range of nearly 6π. All scalebars represent 50 μm.

products of the alloy, specifically magnesium and calcium carbonates and phosphates, as well as hydroxides [63,64]. Beneath that layer is a core from the magnesium alloy. A tomographic representation of this wire and further quantitative analyses were published elsewhere [60]. These findings are further illustrated by the line profiles shown in Fig. 4(b). The profile of the refAP reconstruction (red) follows the form of a (distorted) projected cylinder, as we would expect for the degraded magnesium wire. The unwrapped profile of convAP follows the refractive profile only to a phase shift of -3π. Additionally, the black profile shows the profile of a modified convAP reconstruction. In this case, no unwrapping was applied, which demonstrates the difficulties for conventional PR.

The reconstruction is very challenging for conventional PR methods, for both single-step [54] and iterative algorithms: (i) the two components of the sample, the core and the degradation layer, are different in their optical properties, and (ii) the total phase shift far exceeds 2π. To successfully reconstruct these strongly phase shifting samples, conventional algorithms must be combined with a robust phase unwrapping so that the range clamping and smoothness constraints can be applied. This comes at the price of (strongly) increased computation time. Once again, the refractive representation aids to circumvent the difficulties in the reconstruction.

5. SUMMARY

We have demonstrated how a refractive framework improves PR by directly reconstructing the projected refractive index. The refractive framework avoids the amplitude and phase of the transmission function and instead acts on the real and imaginary parts of the refractive index. This allows to avoid the common phase wrapping problem that occurs if the maximum phase shift of the sample is larger than 2π.

Using the refractive framework, we have derived refractive algorithms for ptychography and holography. We have validated the two algorithms on experimental data from x-ray microscopy. For conventional ptychography and holography, the strongly phase shifting samples are challenging to reconstruct. Phase jumps, especially if there are multiple, are often not accurately reconstructed and can give rise to phase vortices. Removing the vortices requires constant monitoring, as they might reappear in later iterations [65]. In contrast, the refractive variants are able to reconstruct the samples with high fidelity.

The gradients in this work were small enough that not more than one phase wrap per pixel occurred. Strong phase gradients with multiple phase wraps in a single pixel will be challenging to reconstruct even with the refractive framework. The reason is that

large gradients lead directly to large scattering angles. In ptychography, phase gradients larger than π per pixel imply that strong contributions to the diffraction pattern lie outside the detector area. As information will therefore be missing from the measurement, reconstructions will require super-resolution methods [66]. It remains to be tested whether a refractive super-resolution algorithm can reconstruct these strong phase gradients.

As shown in this paper, it is straightforward to implement the refractive framework into existing PR algorithms. Suitable targets are, e.g., multi-slice [8,38] and near-field ptychography [65,67]. With the real and imaginary parts of the refractive index at hand, more sophisticated constraints can be applied to the reconstruction, e.g., the sparsity of the recovered image [68,69]. Multi-wavelength algorithms also benefit from direct access to the refractive index [70,71]. The refractive framework has been successfully applied in a number of use cases [52,60,61,72]. For x-ray microscopy, the refractive framework in combination with the increased coherent flux of fourth generation synchrotron radiation sources will allow to study larger sample volumes at high resolution.

Funding. Deutsche Forschungsgemeinschaft (192346071, SFB 986, project Z2).

Acknowledgment. We acknowledge DESY (Hamburg, Germany), a member of the Helmholtz Association HGF, for the provision of experimental facilities. Parts of this research were carried out at the PETRA III beamlines P05 and P06. Beamtime was allocated for proposal I-20170864 (P05) and as part of the PETRA III inhouse research of D.B. (P06). We thank Berit Zeller-Plumhoff for fruitful discussions and access to the data of the magnesium wire. We thank Imke Greving for fruitful discussions and the support during the beamtime at P05. We thank Jan Garrevoet and Stijn van Malderen for assistance in using P06. S.F. acknowledges financial support from the Deutsche Forschungsgemeinschaft (DFG). This research was supported in part through the Maxwell computational resources operated at DESY and by Ptychography 4.0, a project of the Helmholtz Incubator on Information and Data Science.

Disclosures. The authors declare no conflicts of interest.

Data availability. Data underlying the ptychography results presented in this paper are not publicly available at this time but may be obtained from the authors upon reasonable request. Data underlying the near-field holography results presented in this paper are available in [58].

[†]These authors contributed equally to this work.

REFERENCES

1. J. R. Fienup, "Phase retrieval algorithms: a personal tour [invited]," Appl. Opt. **52**, 45–56 (2012).
2. R. P. Millane, "Phase retrieval in crystallography and optics," J. Opt. Soc. Am. A **7**, 394–411 (1990).
3. L. Taylor, "The phase retrieval problem," IEEE Trans. Antennas Propag. **29**, 386–391 (1981).
4. D. R. Luke, J. V. Burke, and R. G. Lyon, "Optical wavefront reconstruction: theory and numerical methods," SIAM Rev. **44**, 169–224 (2002).
5. Y. Shechtman, Y. C. Eldar, O. Cohen, H. N. Chapman, J. Miao, and M. Segev, "Phase retrieval with application to optical imaging: a contemporary overview," IEEE Signal Process. Mag. **32**, 87–109 (2015).
6. P. A. Midgley and R. E. Dunin-Borkowski, "Electron tomography and holography in materials science," Nat. Mater. **8**, 271–280 (2009).
7. M. Töpperwien, M. Krenkel, K. Müller, and T. Salditt, "Phase-contrast tomography of neuronal tissues: from laboratory-to high resolution synchrotron CT," Proc. SPIE **9967**, 99670T (2016).
8. M. Kahnt, L. Grote, D. Brückner, M. Seyrich, F. Wittwer, D. Koziej, and C. G. Schroer, "Multi-slice ptychography enables high-resolution measurements in extended chemical reactors," Sci. Rep. **11**, 1500 (2021).
9. T. van de Kamp, P. Vagovič, T. Baumbach, and A. Riedel, "A biological screw in a Beetle's leg," Science **333**, 52 (2011).
10. J. Moosmann, A. Ershov, V. Altapova, T. Baumbach, M. S. Prasad, C. LaBonne, X. Xiao, J. Kashef, and R. Hofmann, "X-ray phase-contrast in vivo microtomography probes new aspects of xenopus gastrulation," Nature **497**, 374–377 (2013).
11. N. V. Petrov, A. A. Gorodetsky, and V. G. Bespalov, "Holography and phase retrieval in terahertz imaging," Proc. SPIE **8846**, 88460S (2013).
12. J. Garcia-Sucerquia, W. Xu, S. K. Jericho, P. Klages, M. H. Jericho, and H. J. Kreuzer, "Digital in-line holographic microscopy," Appl. Opt. **45**, 836–850 (2006).
13. H. M. L. Faulkner and J. M. Rodenburg, "Movable aperture lensless transmission microscopy: a novel phase retrieval algorithm," Phys. Rev. Lett. **93**, 023903 (2004).
14. L. Allen, H. Faulkner, M. Oxley, and D. Paganin, "Phase retrieval and aberration correction in the presence of vortices in high-resolution transmission electron microscopy," Ultramicroscopy **88**, 85–97 (2001).
15. M. Beleggia, M. Schofield, V. Volkov, and Y. Zhu, "On the transport of intensity technique for phase retrieval," Ultramicroscopy **102**, 37–49 (2004).
16. K. Giewekemeyer, S. P. Krüger, S. Kalbfleisch, M. Bartels, C. Beta, and T. Salditt, "X-ray propagation microscopy of biological cells using waveguides as a quasipoint source," Phys. Rev. A **83**, 023804 (2011).
17. H. Lichte and M. Lehmann, "Electron holography— basics and applications," Rep. Prog. Phys. **71**, 016102 (2008).
18. M.-C. Zdora, "State of the art of x-ray speckle-based phase-contrast and dark-field imaging," J. Imaging **4**, 60 (2018).
19. F. Pfeiffer, T. Weitkamp, O. Bunk, and C. David, "Phase retrieval and differential phase-contrast imaging with low-brilliance x-ray sources," Nat. Phys. **2**, 258–261 (2006).
20. I. Nesch, D. P. Fogarty, T. Tzvetkov, B. Reinhart, A. C. Walus, G. Khelashvili, C. Muehleman, and D. Chapman, "The design and application of an in-laboratory diffraction-enhanced x-ray imaging instrument," Rev. Sci. Instrum. **80**, 093702 (2009).
21. D. Paganin, S. C. Mayo, T. E. Gureyev, P. R. Miller, and S. W. Wilkins, "Simultaneous phase and amplitude extraction from a single defocused image of a homogeneous object," J. Microsc. **206**, 33–40 (2002).
22. D. Gabor, "A new microscopic principle," Nature **161**, 777–778 (1948).
23. P. Thibault, M. Dierolf, A. Menzel, O. Bunk, C. David, and F. Pfeiffer, "High-resolution scanning x-ray diffraction microscopy," Science **321**, 379–382 (2008).
24. R. W. Gerchberg and W. O. Saxton, "A practical algorithm for the determination of the phase from image and diffraction plane pictures," Optik **35**, 237–246 (1972).
25. M. Guizar-Sicairos, A. Diaz, M. Holler, M. S. Lucas, A. Menzel, R. A. Wepf, and O. Bunk, "Phase tomography from x-ray coherent diffractive imaging projections," Opt. Express **19**, 21345–21357 (2011).
26. M. Stockmar, I. Zanette, M. Dierolf, B. Enders, R. Clare, F. Pfeiffer, P. Cloetens, A. Bonnin, and P. Thibault, "X-ray near-field ptychography for optically thick specimens," Phys. Rev. Appl. **3**, 014005 (2015).
27. A. Gustschin, M. Riedel, K. Taphorn, C. Petrich, W. Gottwald, W. Noichl, M. Busse, S. E. Francis, F. Beckmann, J. U. Hammel, J. Moosmann, P. Thibault, and J. Herzen, "High resolution and sensitivity bi-directional x-ray phase contrast imaging using 2D Talbot array illuminators," Optica **8**, 1588–1595 (2021).
28. S. Chowdhury, M. Chen, R. Eckert, D. Ren, F. Wu, N. Repina, and L. Waller, "High-resolution 3D refractive index microscopy of multiple-scattering samples from intensity images," Optica **6**, 1211–1219 (2019).
29. M. Kahnt, J. Becher, D. Brückner, Y. Fam, T. Sheppard, T. Weissenberger, F. Wittwer, J.-D. Grunwaldt, W. Schwieger, and C. G. Schroer, "Coupled ptychography and tomography algorithm improves reconstruction of experimental data," Optica **6**, 1282–1289 (2019).
30. K. Shimomura, M. Hirose, T. Higashino, and Y. Takahashi, "Three-dimensional iterative multislice reconstruction for ptychographic x-ray computed tomography," Opt. Express **26**, 31199–31208 (2018).
31. A. Ruhlandt, M. Krenkel, M. Bartels, and T. Salditt, "Three-dimensional phase retrieval in propagation-based phase-contrast imaging," Phys. Rev. A **89**, 033847 (2014).
32. J. M. Rodenburg, A. C. Hurst, A. G. Cullis, B. R. Dobson, F. Pfeiffer, O. Bunk, C. David, K. Jefimovs, and I. Johnson, "Hard-x-ray lensless imaging of extended objects," Phys. Rev. Lett. **98**, 034801 (2007).
33. P. Cloetens, W. Ludwig, J. Baruchel, D. Van Dyck, J. Van Landuyt, J. P. Guigay, and M. Schlenker, "Holotomography: quantitative phase tomography with micrometer resolution using hard synchrotron radiation x rays," Appl. Phys. Lett. **75**, 2912–2914 (1999).

34. Y. Jiang, Z. Chen, Y. Han, P. Deb, H. Gao, S. Xie, P. Purohit, M. W. Tate, J. Park, S. M. Gruner, V. Elser, and D. A. Muller, "Electron ptychography of 2D materials to deep sub-ångström resolution," Nature **559**, 343–349 (2018).
35. W. Wirtinger, "Zur formalen Theorie der Funktionen von mehr komplexen Veränderlichen," Math. Ann. **97**, 357–375 (1927).
36. A. M. Maiden and J. M. Rodenburg, "An improved ptychographical phase retrieval algorithm for diffractive imaging," Ultramicroscopy **109**, 1256–1262 (2009).
37. F. Wittwer, "Development and study of refractive phase retrieval and x-ray multibeam ptychography," Ph.d. thesis (Universität Hamburg, 2020).
38. A. M. Maiden, M. J. Humphry, and J. M. Rodenburg, "Ptychographic transmission microscopy in three dimensions using a multi-slice approach," J. Opt. Soc. Am. **29**, 1606–1614 (2012).
39. P. Thibault and A. Menzel, "Reconstructing state mixtures from diffraction measurements," Nature **494**, 68–71 (2013).
40. A. Schropp, D. Brückner, J. Bulda, G. Falkenberg, J. Garrevoet, J. Hagemann, F. Seiboth, K. Spiers, F. Koch, C. David, M. Gambino, M. Veselý, F. Meirer, and C. G. Schroer, "Full-field hard x-ray microscopy based on aberration-corrected be CRLs," Proc. SPIE **11112**, 1111208 (2019).
41. X. Huang, K. Lauer, J. N. Clark, W. Xu, E. Nazaretski, R. Harder, I. K. Robinson, and Y. S. Chu, "Fly-scan ptychography," Sci. Rep. **5**, 9074 (2015).
42. J. Deng, Y. S. G. Nashed, S. Chen, N. W. Phillips, T. Peterka, R. Ross, S. Vogt, C. Jacobsen, and D. J. Vine, "Continuous motion scan ptychography: characterization for increased speed in coherent x-ray imaging," Opt. Express **23**, 5438–5451 (2015).
43. P. M. Pelz, M. Guizar-Sicairos, P. Thibault, I. Johnson, M. Holler, and A. Menzel, "On-the-fly scans for x-ray ptychography," Appl. Phys. Lett. **105**, 251101 (2014).
44. J. N. Clark, X. Huang, R. J. Harder, and I. K. Robinson, "Continuous scanning mode for ptychography," Opt. Lett. **39**, 6066–6069 (2014).
45. P. Godard, M. Allain, V. Chamard, and J. Rodenburg, "Noise models for low counting rate coherent diffraction imaging," Opt. Express **20**, 25914–25934 (2012).
46. C. Yang, J. Qian, A. Schirotzek, F. Maia, and S. Marchesini, "Iterative algorithms for ptychographic phase retrieval," arXiv:1105.5628 (2011).
47. A. Maiden, D. Johnson, and P. Li, "Further improvements to the ptychographical iterative engine," Optica **4**, 736–745 (2017).
48. S. Ruder, "An overview of gradient descent optimization algorithms," arXiv:1609.04747 (2017).
49. Y. E. Nesterov, "A method for solving the convex programming problem with convergence rate $O(1/k^2)$," Dokl. Akad. Nauk SSSR **269**, 543–547 (1983).
50. D. M. Paganin, *Coherent X-Ray Optics* (Oxford University, 2006).
51. P. Vagovič, T. Sato, L. Mikeš, G. Mills, R. Graceffa, F. Mattsson, P. Villanueva-Perez, A. Ershov, T. Faragó, J. Uličný, H. Kirkwood, R. Letrun, R. Mokso, M.-C. Zdora, M. P. Olbinado, A. Rack, T. Baumbach, J. Schulz, A. Meents, H. N. Chapman, and A. P. Mancuso, "Megahertz x-ray microscopy at x-ray free-electron laser and synchrotron sources," Optica **6**, 1106–1109 (2019).
52. J. Hagemann, M. Vassholz, H. Hoeppe, M. Osterhoff, J. M. Rosselló, R. Mettin, F. Seiboth, A. Schropp, J. Möller, J. Hallmann, C. Kim, M. Scholz, U. Boesenberg, R. Schaffer, A. Zozulya, W. Lu, R. Shayduk, A. Madsen, C. G. Schroer, and T. Salditt, "Single-pulse phase-contrast imaging at free-electron lasers in the hard x-ray regime," J. Synchrotron Radiat. **28**, 52–63 (2021).
53. J. Hagemann and T. Salditt, "The fluence–resolution relationship in holographic and coherent diffractive imaging," J. Appl. Crystallogr. **50**, 531–538 (2017).
54. P. Cloetens, R. Barrett, J. Baruchel, J.-P. Guigay, and M. Schlenker, "Phase objects in synchrotron radiation hard x-ray imaging," J. Phys. D **29**, 133–146 (1996).
55. J. Hagemann, M. Töpperwien, and T. Salditt, "Phase retrieval for near-field x-ray imaging beyond linearisation or compact support," Appl. Phys. Lett. **113**, 041109 (2018).
56. D. G. Voelz and M. C. Roggemann, "Digital simulation of scalar optical diffraction: revisiting chirp function sampling criteria and consequences," Appl. Opt. **48**, 6132–6142 (2009).
57. L. M. Lohse, A.-L. Robisch, M. Töpperwien, S. Maretzke, M. Krenkel, J. Hagemann, and T. Salditt, "A phase-retrieval toolbox for x-ray holography and tomography," J. Synchrotron Radiat. **27**, 852–859 (2020).
58. L. M. Lohse, A.-L. Robisch, M. Töpperwien, S. Maretzke, M. Krenkel, J. Hagemann, and T. Salditt, "Holotomotoolbox online repository," 2020, https://gitlab.gwdg.de/irp/holotomotoolbox.
59. F. Witte, "The history of biodegradable magnesium implants: a review," Acta Biomaterialia **6**, 1680–1692 (2010).
60. S. Meyer, A. Wolf, D. Sanders, K. Iskhakova, H. Ćwieka, S. Bruns, S. Flenner, I. Greving, J. Hagemann, R. Willumeit-Römer, B. Wiese, and B. Zeller-Plumhoff, "Degradation analysis of thin Mg-xAg wires using x-ray near-field holotomography," Metals **11**, 1422 (2021).
61. S. Flenner, A. Kubec, C. David, M. Storm, C. F. Schaber, F. Vollrath, M. Müller, I. Greving, and J. Hagemann, "Hard x-ray nano-holotomography with a Fresnel zone plate," Opt. Express **28**, 37514–37525 (2020).
62. R. Cusack and N. Papadakis, "New robust 3-D phase unwrapping algorithms: application to magnetic field mapping and undistorting echoplanar images," NeuroImage **16**, 754–764 (2002).
63. B. Zeller-Plumhoff, M. Gile, M. Priebe, H. Slominska, B. Boll, B. Wiese, T. Würger, R. Willumeit-Römer, and R. H. Meißner, "Exploring key ionic interactions for magnesium degradation in simulated body fluid – a data-driven approach," Corros. Sci. **182**, 109272 (2021).
64. B. Zeller-Plumhoff, H. Helmholz, F. Feyerabend, T. Dose, F. Wilde, A. Hipp, F. Beckmann, R. Willumeit-Römer, and J. U. Hammel, "Quantitative characterization of degradation processes in situ by means of a bioreactor coupled flow chamber under physiological conditions using time-lapse SRμCT," Mater. Corros. **69**, 298–306 (2017).
65. M. Stockmar, P. Cloetens, I. Zanette, B. Enders, M. Dierolf, F. Pfeiffer, and P. Thibault, "Near-field ptychography: phase retrieval for inline holography using a structured illumination," Sci. Rep. **3**, 1927 (2013).
66. A. M. Maiden, M. J. Humphry, F. Zhang, and J. M. Rodenburg, "Superresolution imaging via ptychography," J. Opt. Soc. Am. A **28**, 604–612 (2011).
67. A.-L. Robisch, K. Kröger, A. Rack, and T. Salditt, "Near-field ptychography using lateral and longitudinal shifts," New J. Phys. **17**, 073033 (2015).
68. A. Pein, S. Loock, G. Plonka, and T. Salditt, "Using sparsity information for iterative phase retrieval in x-ray propagation imaging," Opt. Express **24**, 8332–8343 (2016).
69. N. H. Thao, D. R. Luke, O. Soloviev, and M. Verhaegen, "Phase retrieval with sparse phase constraint," SIAM J. Math. Data Sci. **2**, 246–263 (2020).
70. M. Hirose, K. Shimomura, N. Burdet, and Y. Takahashi, "Use of Kramers–Kronig relation in phase retrieval calculation in x-ray spectro-ptychography," Opt. Express **25**, 8593–8603 (2017).
71. A.-L. Robisch, M. Eckermann, M. Töpperwien, F. van der Meer, C. Stadelmann-Nessler, and T. Salditt, "Nanoscale x-ray holotomography of human brain tissue with phase retrieval based on multienergy recordings," J. Med. Imaging **7**, 1 (2020).
72. M. Vassholz, H. P. Hoeppe, J. Hagemann, J. M. Rosselló, M. Osterhoff, R. Mettin, T. Kurz, A. Schropp, F. Seiboth, C. G. Schroer, M. Scholz, J. Möller, J. Hallmann, U. Boesenberg, C. Kim, A. Zozulya, W. Lu, R. Shayduk, R. Schaffer, A. Madsen, and T. Salditt, "Pump-probe x-ray holographic imaging of laser-induced cavitation bubbles with femtosecond FEL pulses," Nat. Commun. **12**, 3468 (2021).
73. V. V. Volkov and Y. Zhu, "Deterministic phase unwrapping in the presence of noise," Opt. Lett. **28**, 2156–2158 (2003).